

Article

Symmetric Diffeomorphic Image Registration with Multi-Label Segmentation Masks

Chenwei Cai ¹, Lvda Wang ² and Shihui Ying ^{1,*} 

¹ Department of Mathematics, School of Sciences, Shanghai University, Shanghai 200444, China; chenweicai@shu.edu.cn

² Beijing Institute of Computer Technology and Applications, Beijing 100036, China; wanglvda@casic.com.cn

* Correspondence: shying@shu.edu.cn

Abstract: Image registration aims to align two images through a spatial transformation. It plays a significant role in brain imaging analysis. In this research, we propose a symmetric diffeomorphic image registration model based on multi-label segmentation masks to solve the problems in brain MRI registration. We first introduce the similarity metric of the multi-label masks to the energy function, which improves the alignment of the brain region boundaries and the robustness to the noise. Next, we establish the model on the diffeomorphism group through the relaxation method and the inverse consistent constraint. The algorithm is designed through the local linearization and least-squares method. We then give spatially adaptive parameters to coordinate the descent of the energy function in different regions. The results show that our approach, compared with the mainstream methods, has better accuracy and noise resistance, and the transformations are more smooth and more reasonable.

Keywords: image registration; diffeomorphic; brain MRI; multi-label segmentation masks; spatially adaptive parameters

MSC: 68U10



Citation: Cai, C.; Wang, L.; Ying, S. Symmetric Diffeomorphic Image Registration with Multi-Label Segmentation Masks. *Mathematics* **2022**, *10*, 1946. <https://doi.org/10.3390/math10111946>

Academic Editor: Jakub Nalepa

Received: 17 May 2022

Accepted: 1 June 2022

Published: 6 June 2022

Publisher's Note: MDPI stays neutral with regard to jurisdictional claims in published maps and institutional affiliations.



Copyright: © 2022 by the authors. Licensee MDPI, Basel, Switzerland. This article is an open access article distributed under the terms and conditions of the Creative Commons Attribution (CC BY) license (<https://creativecommons.org/licenses/by/4.0/>).

1. Introduction

Image registration plays a crucial role in biomedical imaging applications, especially brain imaging analysis. It aims to find a spatial transformation to align datasets across subjects, modalities, or times geometrically. A variety of imaging processing approaches require registration as a preprocessing step. For example, a considerable amount of structural or functional information can be obtained from the brain atlases established from images of a large population [1]. However, it is a great challenge to find potential links between the images because they are of different people, ages, or modalities. We can settle these images through image registration into a standard space where shapes and structures are well aligned. Many subsequent analyses, such as the analysis of anatomical and connectivity patterns, can be performed after image registration [2].

Image registration can be divided into linear and non-linear according to the representation of the transformation. Linear registration methods compute affine transformations. Nevertheless, linear registration generally fails to meet the demands of processing. The reason is that the physiological movements of human bodies may lead to the organs' unregulated changes in position, volume, and shape. Therefore, scholars focus their eyes on non-linear registration because affine transformations cannot describe these changes [3]. Non-linear registration methods are classified into two categories: model-driven and data-driven methods [4]. Model-driven means establishing the explicit expressions of optimization models and then obtaining transformations through optimization methods. In contrast, data-driven approaches do not require explicit expressions. Their main task is to compute the mappings from the image pairs to the transformations [5].

We focus on model-driven methods in our study. The reason is that data-driven methods are prone to overfitting due to the high dimensionality of medical images and the small number of training samples. Under model-driven settings, the transformations can be expressed as simple parametric functions, such as B-spline functions [6–8], radial basis functions [9–11], and thin-plate spline functions [12–14]. The registration models are then turned into parametric optimization models by doing this. The non-parametric treatment is also currently popular. Non-parametric methods consider the registration models as variational problems in which Euler–Lagrange equations should be solved. There are several common non-parametric approaches, such as large deformation diffeomorphic metric mapping (LDDMM) [15–18], elastic registration [19–21], fluid registration [22–24], and diffusion registration [25–27].

Non-parametric methods are more suitable than parametric methods for our research topic on brain magnetic resonance imaging (MRI) registration. We have known a lot of effective methods for brain MRI registration [28–31], which shows that non-parametric methods perform better than parametric methods. The main reason is that non-parametric methods set independent transformation functions at every pixel. Therefore, they have far higher degrees of freedom than parametric methods and can describe the complex deformation of structures in the brain more easily. Moreover, non-parametric methods have many acceleration techniques [32–34], which save the computational time greatly.

However, the existing methods for brain MRI registration have several disadvantages. These methods pay closer attention to the intensity-based local similarity of the images than to the boundary alignment of the brain regions. The complex features of the brain, such as the sulcus gyrus of the cerebral cortex [35], may pull the optimization into local minima. Furthermore, the terminal conditions of these models are based on the average level of the global energy function descent. It easily leads to the situation that some brain regions have not yet been aligned when the iteration stops. Additionally, there is noise in the image acquisition process. These models do not emphasize the robustness to the noise, which can affect the performance in practice.

In this study, we propose a symmetric diffeomorphic image registration method based on multi-label segmentation masks to compensate for the above shortcomings. Firstly, we introduce the similarity metric of the multi-label segmentation masks, i.e., the segmentation result of large regions, into the energy function, which strengthens the alignment of the region boundaries and improves the noise resistance. The acquisition of the masks is not difficult because today's deep learning-based segmentation models [36] offer significant improvements in accuracy and computation time compared to traditional segmentation methods [37–39]. Secondly, we give a selection of spatially adaptive parameters based on the masks. It can prioritize the optimization of both the image similarity metric in the aligned regions and the mask similarity metric in the unaligned regions, so it coordinates the decline of the energy function spatially. Thirdly, we design an effective approximation algorithm through model relaxation, least-squares method, etc. We validate the effectiveness of our method in three different experiments. The results show that our method has better accuracy and robustness compared to the mainstream approaches, and meanwhile, the deformation field retains excellent reversibility, smoothness, and reasonableness.

2. Materials and Methods

2.1. Mathematical Background Knowledge

Let $F, M : \Omega \rightarrow [0, 1]$ denote the **fixed image** and the **moving image**, respectively. The domain of the images is $\Omega \subset \mathbb{R}^n$, where $n = 2$ for 2D images and $n = 3$ for 3D images. The task of the non-linear image registration is to compute a **deformation field** (transformation) $\varphi : \Omega \rightarrow \Omega$ to make the warped moving image $M \circ \varphi$ as similar as possible to the fixed image F . In the setting of non-parametric registration, the deformation field is expressed as $\varphi = \mathbf{Id} - u$, where \mathbf{Id} is the identity map and u is called the displacement field of φ .

The accuracy of the transformation is measured by a **similarity metric** E_1 , which often takes the form of the sum of squared difference (SSD) $E_1(\varphi) = \|M \circ \varphi - F\|_{L_2}^2$. In addition, the transformation is required to have the presupposed properties, which are measured by a **regularization term** E_2 . The most common property is the global smoothness, i.e., L_2 regularization expressed as $E_2(\varphi) = \|\nabla\varphi\|_{L_2}^2$. The registration problem is written as

$$\min_{\varphi} E(\varphi) = \frac{1}{\sigma^2} E_1 + E_2 = \frac{1}{\sigma^2} \|M \circ \varphi - F\|^2 + \|\nabla\varphi\|^2, \tag{1}$$

where $1/\sigma^2$ is a positive number that controls the balance between E_1 and E_2 . We omit the notation L_2 for simplicity.

The solution space of this problem can be restricted to the **diffeomorphism group** $\text{Diff}(\Omega) = \{\varphi | \varphi^{-1} \text{ exists and } \varphi, \varphi^{-1} \in C^\infty(\Omega, \Omega)\}$, which is a Lie group. Any tangent vector $v \in V$ of $\varphi_0 = \text{Id}$ is a vector field on Ω , where $V = T_{\text{Id}}\text{Diff}(\Omega)$ is a Lie algebra. We often call v a **velocity field** in the research fields of registration [4]. A diffeomorphism can be generated by the **exponential map** on $\text{Diff}(\Omega)$, i.e., $\varphi = \exp(v)$. It provides the **intrinsic update step** [40,41] on the diffeomorphism group:

$$\varphi \leftarrow \varphi \circ \exp(v), \tag{2}$$

where v is the velocity field update, and \circ is both the function composition and the multiplication on the Lie group.

A practical method to compute the exponential map of vector fields, given by Arsigny et al. [42], is based on the idea of “scaling and squaring” [43]. For any integer N , it holds $\exp(v) = (\exp(N^{-1}v))^N$ because of the property of the exponential map, i.e., $\exp((t_1 + t_2)v) = \exp(t_1v) \cdot \exp(t_2v)$ for any $t_1, t_2 \in \mathbb{R}$. Suppose v is a small vector field, it is reasonable to use the first-order approximation of the exponential map. We denote $w = \exp(v)$ as the result transformation, and the algorithm of the exponential map is described as follows (Algorithm 1).

Algorithm 1 The first-order algorithm for the exponential map of vector fields

- Choose a proper N such that $2^{-N}v$ is close enough to $\mathbf{0}$, e.g., $\max_x \|2^{-N}v(x)\| \leq 0.5$.
 - Implement the first-order integration: $w(x) = 2^{-N}v(x)$ for every $x \in \Omega$.
 - Do N recursive squarings: $w \leftarrow w \circ w$.
-

Therefore, in the above setting, the velocity field update of each iteration is selected in V discretely, and the result velocity field is regarded as a constant. We often call it a **stationary velocity field** (SVF). By contrast, the velocity field of LDDMM [15–18] varies over time, i.e., $v = v_t$ is a continuous curve in V . The SVF methods, such as Diffeomorphic Demons [27] and Log-domain Diffeomorphic Demons [44], do not optimize the global variational problem like LDDMM because they do not update the velocity field in the whole time flow. However, the SVF methods have less computational cost and can thus obtain a diffeomorphism quickly.

2.2. The Reassignment of the Segmentation Masks

We can improve the boundary alignment of brain regions and the robustness to the noise through the multi-label segmentation masks of large regions, which are the regions of white matter (WM), grey matter (GM), and cerebrospinal fluid (CSF). The masks are available easily because there is an obvious difference in the intensity values (see Figure 1).

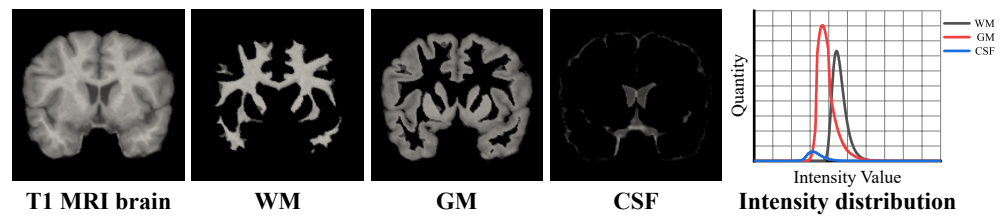


Figure 1. A T1 MRI human brain image, tissue segmentation, and corresponding intensity distributions are shown.

We propose reassigning the intensity values on the masks. Suppose there are m images participating in the registration, we set the intensity value of the r -th region to be

$$B_r = \frac{1}{m} \sum_{j=1}^m \frac{1}{|\Omega_r^j|} \int_{\Omega_r^j} I_j(x) dx, \tag{3}$$

where B is the segmentation mask, I_j is the j -th image, and Ω_r^j is the r -th region on I_j . It means we first average the intensity value on the region of one image and then average among different images. For example, we assume to use only two images I_1, I_2 , and there are two regions on the images. The average intensity values of the first region of I_1, I_2 are $B_1^1 = \frac{1}{|\Omega_1^1|} \int_{\Omega_1^1} I_1(x) dx, B_1^2 = \frac{1}{|\Omega_1^2|} \int_{\Omega_1^2} I_2(x) dx$, respectively. We then obtain the average intensity value on the first region, i.e., $B_1 = \frac{1}{2} (B_1^1 + B_1^2)$. Therefore, we calculate the intensity values of the segmentation masks once throughout the process. Significantly, we need histogram matching [45] on the images before the reassignment because we should avoid the gap of the intensity values in the same region among different images.

We add the information of the average intensity values of the regions to the masks through the reassignment. Consequently, the intensity magnitude of the masks coincides with that of the images. The spatial information of the region boundaries is also retained. Furthermore, we can improve the robustness to the noise by the reassignment. The reason is that the intensity values of the contaminated pixels are pulled back towards the average values on the regions when we introduce the similarity metric of the masks to the energy function. Therefore, the influence of the noise is weakened, and we improve the anti-noise ability of the model by doing this.

2.3. The Proposed Model

Firstly, we take the SSD as the similarity metric and the L_2 smoothness as the regularization term. In the integral form, the energy function is

$$E(\varphi) = \frac{1}{\sigma^2} E_1 + E_2 = \int_{\Omega} \frac{1}{\sigma^2} \|M(\varphi(x)) - F(x)\|^2 + \|\nabla \varphi(x)\|^2 dx. \tag{4}$$

We restrict the solution space to the diffeomorphism group $\mathbf{Diff}(\Omega)$. Therefore, we introduce the energy of the inverse transformation to ensure reversibility. The energy function is then extended to a symmetric form with the transformation and the inverse transformation as variables. We denote ψ as the slack variable of φ^{-1} and reformulate the energy function, Equation (4), as

$$E(\varphi, \psi) = \int_{\Omega} \frac{1}{\sigma^2} (\|M(\varphi(x)) - F(x)\|^2 + \|F(\psi(x)) - M(x)\|^2) + \|\nabla \varphi(x)\|^2 + \|\nabla \psi(x)\|^2 dx, \tag{5}$$

$$s.t. \quad \varphi \circ \psi = \mathbf{Id}, \psi \circ \varphi = \mathbf{Id}, \varphi, \psi \in \mathbf{Diff}(\Omega). \tag{6}$$

Next, we penalize Equation (6) to the energy function Equation (5), i.e., we add the inverse consistent constraint [46,47]

$$E_3(\varphi, \psi) = \int_{\Omega} \|(\mathbf{Id} - \varphi \circ \psi)(x)\|^2 + \|(\mathbf{Id} - \psi \circ \varphi)(x)\|^2 dx. \tag{7}$$

We tie φ and ψ together in the energy function by doing this. $\|(\mathbf{Id} - \varphi \circ \psi)(x)\|^2$ and $\|(\mathbf{Id} - \psi \circ \varphi)(x)\|^2$ are of no difference mathematically because of $\varphi \circ \psi = \psi \circ \varphi = \mathbf{Id}$. However, we should retain both of them because there is an error between ψ and φ^{-1} , which will be amplified during calculation. Moreover, keeping E_3 symmetric can reduce the difficulty of solving because we can divide them into two subproblems later.

After that, we introduce the similarity metric of the multi-label segmentation masks. We denote $B_F, B_M : \Omega \rightarrow [0, 1]$ as the segmentation masks of the fixed image F and the moving image M , respectively. The magnitude of B_F and B_M is consistent with that of the images because we have carried out the reassignment of the masks. We use the symmetric SSD form, i.e.,

$$E_4(\varphi, \psi) = \int_{\Omega} \|B_M(\varphi(x)) - B_F(x)\|^2 + \|B_F(\psi(x)) - B_M(x)\|^2 dx. \tag{8}$$

Minimizing E_4 helps the alignment of the region boundaries. It should be noted that the segmentation masks are different from the images even if they both take the SSD form. The reason is that the intensity value of the segmentation masks is a constant within one region, leading to $E_4 = 0$. Therefore, there is little force to cause deformation in the overlap of B_F and B_M when E_1 is not involved in the registration.

Finally, we integrate Equations (5), (7) and (8) to formulate our model:

$$\min_{\varphi, \psi} E = \frac{1}{\sigma_1^2} E_1 + E_2 + \frac{1}{\sigma_3^2} E_3 + \frac{1}{\sigma_2^2} E_4 \tag{9}$$

where $1/\sigma_1^2$, $1/\sigma_2^2$ and $1/\sigma_3^2$ are positive numbers controlling the influence of E_1 , E_4 and E_3 , respectively.

2.4. Numerical Implementation

Firstly, we split the registration problem Equation (9) into two subproblems so that the alternating iteration strategy can be applied.

$$\begin{aligned} \psi^{k+1} = \arg \min_{\psi} H_1^k := & \int_{\Omega} \frac{1}{\sigma_1^2} \|F(\psi(x)) - M(x)\|^2 + \frac{1}{\sigma_2^2} \|B_F(\psi(x)) - B_M(x)\|^2 \\ & + \frac{1}{\sigma_3^2} \|(\mathbf{Id} - \varphi^k \circ \psi)(x)\|^2 + \|\nabla \psi(x)\|^2 dx, \end{aligned} \tag{10}$$

$$\begin{aligned} \varphi^{k+1} = \arg \min_{\varphi} H_2^k := & \int_{\Omega} \frac{1}{\sigma_1^2} \|M(\varphi(x)) - F(x)\|^2 + \frac{1}{\sigma_2^2} \|B_M(\varphi(x)) - B_F(x)\|^2 \\ & + \frac{1}{\sigma_3^2} \|(\mathbf{Id} - \psi^k \circ \varphi)(x)\|^2 + \|\nabla \varphi(x)\|^2 dx. \end{aligned} \tag{11}$$

where k is the number of external iterations.

Next, we consider only the subproblem Equation (11) in the following steps because Equation (10) can be solved in the same way. We introduce a slack variable c to avoid hard point-to-point correspondences following the strategy of Cachier et al. [48]. Consequently, we turn the subproblem Equation (11) into

$$\begin{aligned} \min_{\varphi, c} H_2^k := & \int_{\Omega} \frac{1}{\sigma_1^2} \|M(c(x)) - F(x)\|^2 + \frac{1}{\sigma_2^2} \|B_M(c(x)) - B_F(x)\|^2 + \frac{1}{\sigma_3^2} \|(\mathbf{Id} - \psi^k \circ c)(x)\|^2 \\ & + \frac{1}{\sigma_x^2} \|(\varphi - c)(x)\|^2 + \|\nabla \varphi(x)\|^2 dx. \end{aligned} \tag{12}$$

where $1/\sigma_x^2$ controls the spatial correspondence error. We can separate Equation (12) further into two new subproblems:

$$c^{k,l+1} = \arg \min_c L_1^{k,l} := \int_{\Omega} \frac{1}{\sigma_1^2} \|M(c(x)) - F(x)\|^2 + \frac{1}{\sigma_2^2} \|B_M(c(x)) - B_F(x)\|^2 + \frac{1}{\sigma_3^2} \left\| \left(\mathbf{Id} - \psi^k \circ c \right) (x) \right\|^2 + \frac{1}{\sigma_x^2} \left\| (\varphi^{k,l} - c)(x) \right\|^2 dx, \tag{13}$$

$$\varphi^{k,l+1} = \arg \min_{\varphi} L_2^{k,l} := \int_{\Omega} \frac{1}{\sigma_2^2} \left\| (\varphi - c^{k,l+1})(x) \right\|^2 + \|\nabla \varphi(x)\|^2 dx, \tag{14}$$

where l is the number of internal iterations. In addition, we will use the approximation of $\left\| \left(\mathbf{Id} - \psi^k \circ c \right) (x) \right\|^2$ in Equation (13), i.e., applying the fixed image F on it, which changes it to

$$\left\| F(x) - F\left(\psi^k \circ c(x)\right) \right\|^2. \tag{15}$$

It can match the magnitude of this item with that of the images and the masks.

After that, we use the first-order approximation of the intrinsic update step $c = \varphi^{k,l} \circ \exp\left(v^{k,l}\right)$ to simplify Equation (13), where $v^{k,l}$ is the update velocity field. The approximation is reasonable because $v^{k,l}$ is small. Therefore, Equation (13) becomes

$$L_1^{k,l}(v^{k,l}) \approx \int_{\Omega} \frac{1}{\sigma_1^2} \left\| J_{\varphi^{k,l}}^M(x)v^{k,l}(x) - FM(x) \right\|^2 + \frac{1}{\sigma_2^2} \left\| J_{\varphi^{k,l}}^{B_M}(x)v^{k,l}(x) - B_F B_M(x) \right\|^2 + \frac{1}{\sigma_3^2} \left\| J_{\psi^k \circ \varphi^{k,l}}^F(x)v^{k,l}(x) - FF(x) \right\|^2 + \frac{1}{\sigma_x^2} \left\| v^{k,l}(x) \right\|^2 dx, \tag{16}$$

where $J_f^A(x) = \nabla^T A(f(x))$ is a row vector, and

$$FM(x) = F(x) - M\left(\varphi^{k,l}(x)\right), \tag{17}$$

$$B_F B_M(x) = B_F(x) - B_M\left(\varphi^{k,l}(x)\right), \tag{18}$$

$$FF(x) = F(x) - F\left(\psi^k \circ \varphi^{k,l}(x)\right). \tag{19}$$

We can rewrite Equation (16) as the following least-squares problem:

$$\min_{v^{k,l}} L_1^{k,l}(v^{k,l}) \approx \int_{\Omega} \left\| \begin{pmatrix} \frac{1}{\sigma_1} J_{\varphi^{k,l}}^M \\ \frac{1}{\sigma_2} J_{\varphi^{k,l}}^{B_M} \\ \frac{1}{\sigma_3} J_{\psi^k \circ \varphi^{k,l}}^F \\ \frac{1}{\sigma_x} I \end{pmatrix} v^{k,l} - \begin{pmatrix} \frac{1}{\sigma_1} FM \\ \frac{1}{\sigma_2} B_F B_M \\ \frac{1}{\sigma_3} FF \\ 0 \end{pmatrix} \right\|^2 dx, \tag{20}$$

where I is the identity matrix of size n .

Finally, we obtain the least-squares solution of Equation (20) through the Sherman–Morrison formula:

$$v^{k,l} = \frac{\frac{1}{\sigma_1^2} FM \cdot J_{\varphi^{k,l}}^M + \frac{1}{\sigma_2^2} B_F B_M \cdot J_{\varphi^{k,l}}^{B_M} + \frac{1}{\sigma_3^2} FF \cdot J_{\psi^k \circ \varphi^{k,l}}^F}{\frac{1}{\sigma_1^2} \left\| J_{\varphi^{k,l}}^M \right\|^2 + \frac{1}{\sigma_2^2} \left\| J_{\varphi^{k,l}}^{B_M} \right\|^2 + \frac{1}{\sigma_3^2} \left\| J_{\psi^k \circ \varphi^{k,l}}^F \right\|^2 + \frac{1}{\sigma_x^2}}, \tag{21}$$

where we omit the position x for simplicity. Similarly, we can solve the least-squares problem acquired from Equation (10) from the above steps:

$$s^{k,l} = \frac{\frac{1}{\sigma_1^2} MF \cdot J_{\psi^{k,l}}^F + \frac{1}{\sigma_2^2} B_M B_F \cdot J_{\psi^{k,l}}^{B_F} + \frac{1}{\sigma_3^2} MM \cdot J_{\varphi^k \circ \psi^{k,l}}^M}{\frac{1}{\sigma_1^2} \|J_{\psi^{k,l}}^F\|^2 + \frac{1}{\sigma_2^2} \|J_{\psi^{k,l}}^{B_F}\|^2 + \frac{1}{\sigma_3^2} \|J_{\varphi^k \circ \psi^{k,l}}^M\|^2 + \frac{1}{\sigma_x^2}}, \tag{22}$$

where $s^{k,l}$ is the update velocity field of $\psi^{k,l}$, and

$$MF(x) = M(x) - F(\psi^{k,l}(x)), \tag{23}$$

$$B_M B_F(x) = B_M(x) - B_F(\psi^{k,l}(x)), \tag{24}$$

$$MM(x) = M(x) - M(\varphi^k \circ \psi^{k,l}(x)). \tag{25}$$

As for the new subproblem Equation (14), we can obtain the closed-form solution with a Gaussian convolution, i.e., $\varphi^{k,l+1} = K * (\varphi^{k,l} \circ \exp(v^{k,l}))$, where K is a Gaussian kernel. This is because of the special form of the regularization term [49]. Consequently, the closed-form solution of the subproblem Equation (10) is also obtained: $\psi^{k,l+1} = K * (\psi^{k,l} \circ \exp(s^{k,l}))$.

The algorithm of our proposed method is as follows (Algorithm 2).

Algorithm 2 Symmetric diffeomorphic image registration with multi-label segmentation masks

```

Initialize  $\varphi, \psi, v, s$ .
repeat
  {Update the backward transform  $\psi$ }
  repeat
    Compute the velocity field  $s$  using Equation (22).
     $s \leftarrow K_{fluid} * s$  (fluid-like regularization).
     $c \leftarrow \psi \circ \exp(s)$  (intrinsic update step using Algorithm 1).
     $\psi \leftarrow K_{diff} * c$  (diffusion-like regularization).
  until Convergence
  {Update the forward transform  $\varphi$ }
  repeat
    Compute the velocity field  $v$  using Equation (21).
     $v \leftarrow K_{fluid} * v$  (fluid-like regularization).
     $c \leftarrow \varphi \circ \exp(v)$  (intrinsic update step using Algorithm 1).
     $\varphi \leftarrow K_{diff} * c$  (diffusion-like regularization).
  until Convergence
until Convergence
    
```

2.5. The Selection of Spatially Adaptive Parameters

In this section, we consider only the parameters in Equation (21) because we can acquire those in Equation (22) similarly.

Firstly, we need to review the traditional selection of parameters based on statistics. We assume that $\{FM(x) | x \in \Omega\}$ is independent and identically distributed (IID) in a normal distribution $N(0, \sigma_1^2)$. This setting is reasonable when Ω is huge because of the Lindberg–Lévy central limit theorem. We choose the zero mean because we hope that the warped moving image fully aligns with the fixed image. We write the likelihood function, based on the maximum likelihood estimation (MLE), as

$$W = \prod_x \frac{1}{\sqrt{2\pi}\sigma_1} \exp\left\{-\frac{FM(x)^2}{2\sigma_1^2}\right\}. \tag{26}$$

The optimal estimation of σ_1^2 is obtained through $-\partial \ln(W)/\partial \sigma_1 = 0$, i.e.,

$$\sigma_1^2 = \frac{1}{|\Omega|} \int_{\Omega} \|FM(x)\|^2 dx, \tag{27}$$

where $|\Omega|$ is the area of Ω . In particular, we can regard Ω as the neighborhood of a specific position x , denoted as Ω_x , where we can change the radius of it arbitrarily. The extreme condition is when the radius is zero, leading to $\sigma_1^2(x) = \|FM(x)\|^2$, which is the selection of Thirion [50]. This parameter not only adjusts the influence between the similarity metric and the regularization term dynamically but also controls the magnitude of E_1 by transferring the distribution of $FM(x)/\sigma_1$ to $N(0, 1)$.

Next, we evaluate the misalignment based on the multi-label segmentation masks. We treat $B_F B_M(x)$ as a continuous random variable. The reason is that the activation functions [51], such as the Sigmoid function and the *tanh* function, can smooth the gap around the area boundaries, although $B_F B_M(x)$ can take only some values. We denote $\mathbb{1}$ as the indicator function, which fulfills $\mathbb{1}(x) = 1$ if $x > 0$ and $\mathbb{1}(x) = 0$ if $x = 0$. We then introduce the probability of misalignment based on the masks:

$$p(x) = \frac{1}{|N_x|} \int_{N_x} \mathbb{1}(B_F B_M(y)) dy, \tag{28}$$

where N_x is the neighborhood of x . The indicator function helps distinguish whether the alignment improves or the low-intensity values occur when $B_F B_M(y)$ declines. This probability p is especially a widely used overlap metric called the “target overlap” [28] when N_x is large enough to cover $\Omega_{B_F}^r$, i.e., $p = |\Omega_{B_F}^r \cap \Omega_{B_M}^r| / |\Omega_{B_F}^r|$, where r is the index of the regions.

After that, we give our selection of spatially adaptive parameters. We think that $1/\sigma_i^2$, $i = 1, 2, 3$ are connected because the decline of E_1 and E_3 is not meaningful unless the alignment of region boundaries is good. Therefore, the parameters should satisfy two requirements:

- When the alignment is poor (p approaches 1), we reduce the effect of E_1 and E_3 and increase that of E_4 . When the alignment is good (p approaches 0), we do the opposite.
- The role of E_1 should be stronger than that of E_3 because the decline of E_3 cannot improve registration accuracy.

Therefore, we denote the parameters as functions of p , i.e., $1/\sigma_i^2 = q_i(p)$. Specifically, we define

$$q_1 = c_1(1 - p), \quad c_1 = \frac{1}{|N_x|} \int_{N_x} \|B_F B_M(y)\|^2 dy, \tag{29}$$

$$q_2 = c_2 p, \quad c_2 = \frac{1}{|N_x|} \int_{N_x} \|FM(y)\|^2 dy, \tag{30}$$

$$q_3 = \lambda q_1, \tag{31}$$

where $\lambda \in [0, 1]$, and c_1 and c_2 are the MLEs of $1/\sigma_1^2$ and $1/\sigma_2^2$ (see Equation (27)), respectively. We denote the radius of N_x as R . The parameters, λ and R , are both determined by the user because the influence of E_3 on E_1 and the amount of computation vary in different tasks. It is worth noting that we need to add a small positive number to the denominator of c_i when c_i is not well defined.

Finally, we validate the effectiveness of the parameters. When $0 < p < 1$, we express the ratio of the importance between the similarity metric of the images and that of the masks, i.e., the ratio of E_1 to E_4 , as

$$\frac{q_1}{q_2} = \left(\frac{1}{p} - 1\right) \frac{\int_{N_x} \|FM(y)\|^2 dy}{\int_{N_x} \|B_F B_M(y)\|^2 dy}. \tag{32}$$

We know that $\int_{N_x} \|FM(y)\|^2 dy$ is constant when x is fixed. Meanwhile, we infer that p and $\int_{N_x} \|B_F B_M(y)\|^2 dy$ are positively related based on Equation (28). We thus conclude from Equation (32) that q_1/q_2 decreases when p increases, which means E_4 plays a key role; q_1/q_2 increases when p decreases, which means E_1 plays a key role. Therefore, the parameters vary according to the current position and the decline of the energy function, which coordinates the optimization process spatially.

3. Results

In this section, we evaluate the performance of our method with three experiments. The experimental images include synthetic 2D images, the OASIS-1 dataset [52], and the IBSR18 dataset [53]. All these experiments are implemented using C++ in a Ubuntu 16 system, with two Intel Xeon Silver 4216 @2.1GHz CPUs and 128GB 2666MHz memory.

3.1. Implementation Details and Algorithmic Comparison

Firstly, we regard our algorithm’s user-determined parameters. We choose the radius of N_x to be $R = 1$ considering the calculation time. We select $\lambda = 0.5$, which means the ratio of E_1 to E_3 is 2 : 1. In addition, the algorithm has two terminal conditions, i.e., the maximum iterations and the minimum magnitude of the update step.

Next, we implement the algorithm based on the open-source library Insight Toolkit (ITK) 5.1 (<https://itk.org>, accessed on 31 May 2022). We use the combination of two itkPDEDeformableRegistrationFilters to iterate alternatively, as shown in Figure 2a. There are four modules in itkPDEDeformableRegistrationFilter, as shown in Figure 2b. We denote two Gaussian kernels as K_{fluid} and K_{diff} , where K_{fluid} smooths the update field and K_{diff} smooths the deformation field. The exponential map is computed through itkExponentialDisplacementFieldImageFilter. All modules are set to compute parallelly by the multithreading technique [54].

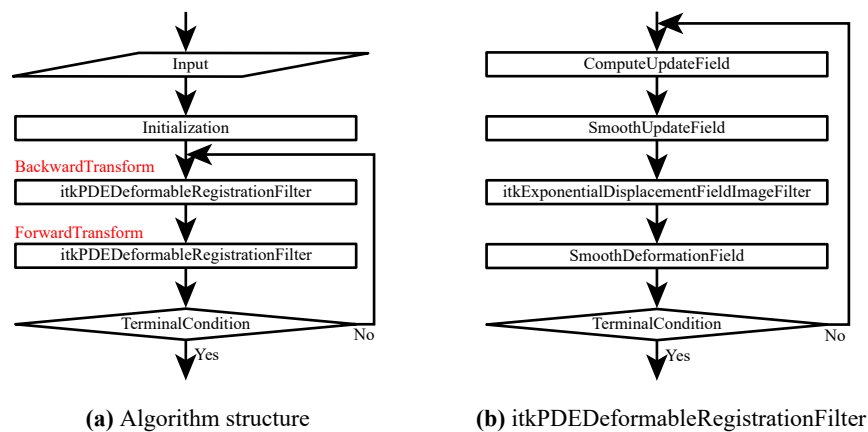


Figure 2. (a) The structure of the whole algorithm. (b) The structure of itkPDEDeformableRegistrationFilter.

After that, we use two mainstream approaches for comparison, i.e., Diffeomorphic Demons and SyN. Vercauteren et al. [27], who proposed Diffeomorphic Demons, applied the SVF framework to the classic Demons algorithm [55], enhancing the smoothness and deformability of the transformations. SyN is a symmetric diffeomorphic registration method, which uses the local correlation coefficient (LCC) as the similarity metric. Avants et al. [56] provided the SyN approach based on the LDDMM algorithm [15], strengthening the registration accuracy and reversibility. Diffeomorphic Demons and SyN are both widely used to compare with the brain registration methods [28]. In addition, K_{fluid} and K_{diff} are also used in these two approaches.

Finally, we introduce the algorithmic comparison and related notations. We denote our method as **Ours**, our method without the inverse consistent constraint as **Ours-NId**,

and our method without the similarity metric of the masks as **Ours-NSeg**. We also denote Diffeomorphic Demons [27] as **DiffDe** and SyN [56] as **SyN**. In addition, we denote the number of iterations as **numIt** and denote two Gaussian kernels K_{fuilid} and K_{diff} as **Kf σ** and **Kd σ** , respectively, where σ is the standard deviation (**stDev**). All methods are performed only once at the highest resolution of the images for fairness. Moreover, we introduce the following five evaluation metrics considering accuracy, reversibility, reasonability, and smoothness.

- *Accuracy*: The Dice ratio (**DR**(Ω)) [28] is defined by

$$\frac{2 \sum_r |\Omega_{B_F}^r \cap \Omega_{B_M}^r|}{\sum_r (|\Omega_{B_F}^r| + |\Omega_{B_M}^r|)}, \tag{33}$$

where r is the index of the regions, and $|\cdot|$ is the volume. It is a measure of region overlap, which should be as high as possible.

- *Reversibility*: The identity error (**IdErr**) is defined by $\frac{1}{|\Omega|} \|\text{Id} - \varphi \circ \psi\|^2$. It reflects the difference between the identity map and the composition of the forward and backward transformation, which should be as low as possible.
- *Reasonability*: The probability of negative Jacobian determinant of the transformation (**P(DetJ)**) [57] is defined as $\frac{1}{|\Omega|} \mathbb{1}(-\text{Det}(J\varphi))$, where $J\varphi$ is the Jacobian of the transformation, and $\mathbb{1}$ is the indicator function, which fulfills $\mathbb{1}(x) = 1$ if $x > 0$ and $\mathbb{1}(x) = 0$ if $x \leq 0$. It measures how frequently φ is not isomorphic locally, which should be as low as possible.
- *Smoothness*: The maximum Jacobian determinant of the transformation (**M(DetJ)**) is defined as $\max_{\Omega} \text{Det}(J\varphi)$. It computes the upper limit of the sharpest deformation, which should be as low as possible.
- *Smoothness*: The smoothness error (**SMErr**) is defined by $\frac{1}{|\Omega|} \|\nabla\varphi\|^2$. It measures the mean value of the L_2 norm of the gradient field, which should be as low as possible.

Furthermore, we denote the masks of WM, GM, and CSF segmentation as **WGCS**, which are the multi-label segmentation masks B_F and B_M . We denote the detailed masks of brain regions' segmentation as **BRS**, which are used for computing the Dice ratio.

3.2. The Ablation Experiments on Synthetic 2D Data

In this section, we conduct ablation experiments to verify the effectiveness of E_3 and E_4 , i.e., the inverse consistent constraint and the similarity metric of the masks. The synthetic 2D data, with the size of 100×100 , is a simple simulation of the brain, as shown in the first row of Figure 3. We generate the fixed image first with three ellipses of the same center. Then, we set the asymptotic intensity values to avoid being the same as the masks, as shown in the second row of Figure 3. We produce the moving image last by changing the long and short axes, which mimics the possible deformation in the brain [58]. We also apply a shear transform towards the x -axis with 84° to test the ability to recover simple linear transformations.

We will carry out registration with **numIt** = 300, which makes the optimization process converged. In particular, we set 20 external iterations \times 15 internal iterations in our method. Moreover, we select two kinds of smoothing parameters, i.e., **Kf2 Kd0.5** and **Kf1 Kd1**. The reason to select **Kf1 Kd1** is that it is the same as the classic **DiffDe** [27], and many methods verify its effectiveness. By contrast, **Kf2 Kd0.5** is a compromise between the standard setting of **DiffDe** and **SyN** [59]. Since **DiffDe** cannot obtain the inverse transformation in one registration, it performs an additional backward registration, i.e., exchanging M and F . The qualitative results are shown in Figure 4, and the quantitative results are shown in Tables 1 and 2.

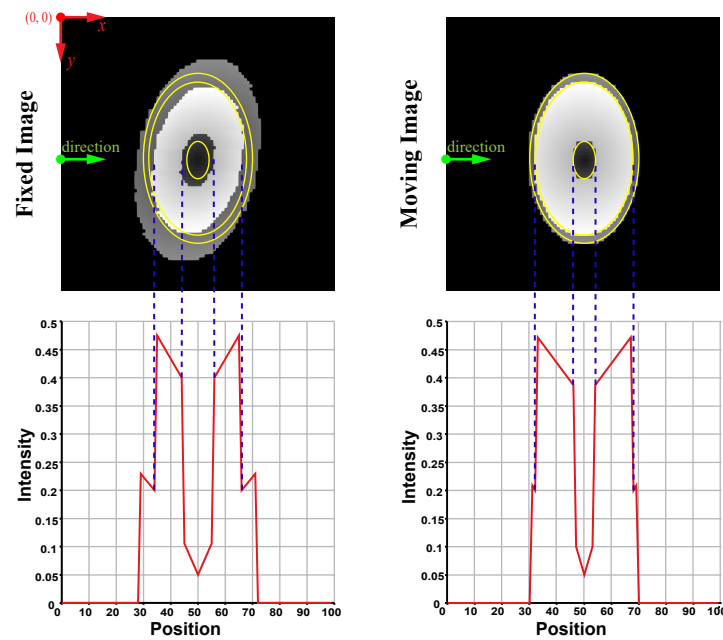


Figure 3. The synthetic 2D data in Section 3.2 is shown. The first row displays the moving and fixed images. The boundaries of the fixed image are marked with yellow outlines. The second row plots the images of the intensity value on the line segment from (0, 50) to (99, 50), which is the direction of the green arrows.

Firstly, we discuss, based on Figure 4, the effect of the smoothing parameters. The standard deviations of \mathbf{Kf} and \mathbf{Kd} determine the sharpness of the deformation, as shown in the magnitude images of the transformations. It reveals that \mathbf{Kd} affects smoothness the most because the higher the \mathbf{stDev} of \mathbf{Kd} , the smoother the transformation. In addition, the results of $\mathbf{Kf2 Kd0.5}$ are better than those of $\mathbf{Kf1 Kd1}$, as shown in the warped moving images and the residual images. It suggests that low \mathbf{stDevs} lead to more accurate results. Therefore, we should choose the smoothing parameters carefully in practice to balance accuracy and smoothness.

Secondly, we discuss, based on Tables 1 and 2, the results of the ablation experiments. **Ours-NSeg** shows excellent results in the items of \mathbf{IdErr} , $\mathbf{M(DetJ)}$, and \mathbf{SMErr} , but the \mathbf{DR} is relatively low. However, the behavior of **Ours-NId** is just the opposite. We conclude that the similarity metric of the masks improves the accuracy, and the inverse consistent constraint improves the reversibility, reasonability, and smoothness. Therefore, the good results of **Ours** shows it combines the advantages of both E_3 and E_4 .

Table 1. The quantitative results of Section 3.2 with smoothing parameters $\mathbf{Kf1 Kd1}$ are shown. The first row lists the methods, and the second to the fifth rows represent the Dice ratio (\mathbf{DR}), the identity error (\mathbf{IdErr}), the maximum Jacobian determinant of the transformations ($\mathbf{M(DetJ)}$), and the smoothness error (\mathbf{SMErr}), respectively. The numbers with wavy lines are the best among **Ours-NSeg**, **Ours-NId**, and **Ours**. The bolded numbers are the best among **DiffDe**, **SyN**, and **Ours**.

	DiffDe	SyN	Ours-NSeg	Ours-NId	Ours
DR	0.890	0.824	0.805	0.900	0.901
IdErr	0.364	0.001	<u>0.018</u>	0.094	0.040
M(DetJ)	2.962	3.206	<u>1.533</u>	2.611	2.643
SMErr	0.082	0.017	<u>0.002</u>	0.061	0.060

Table 2. The quantitative results of Section 3.2 with smoothing parameters **Kf2 Kd0.5** are shown. The first row lists the methods, and the second to the fifth rows represent the same evaluation metrics as Table 1. The numbers with wavy lines are the best among **Ours-NSeg**, **Ours-NId**, and **Ours**. The bolded numbers are the best among **DiffDe**, **SyN**, and **Ours**.

	DiffDe	SyN	Ours-NSeg	Ours-NId	Ours
DR	0.931	0.944	0.884	<u>0.960</u>	<u>0.960</u>
IdErr	0.543	0.125	<u>0.035</u>	0.218	<u>0.136</u>
M(DetJ)	4.003	5.511	<u>2.487</u>	3.770	3.866
SMErr	0.231	0.577	<u>0.038</u>	0.271	0.267

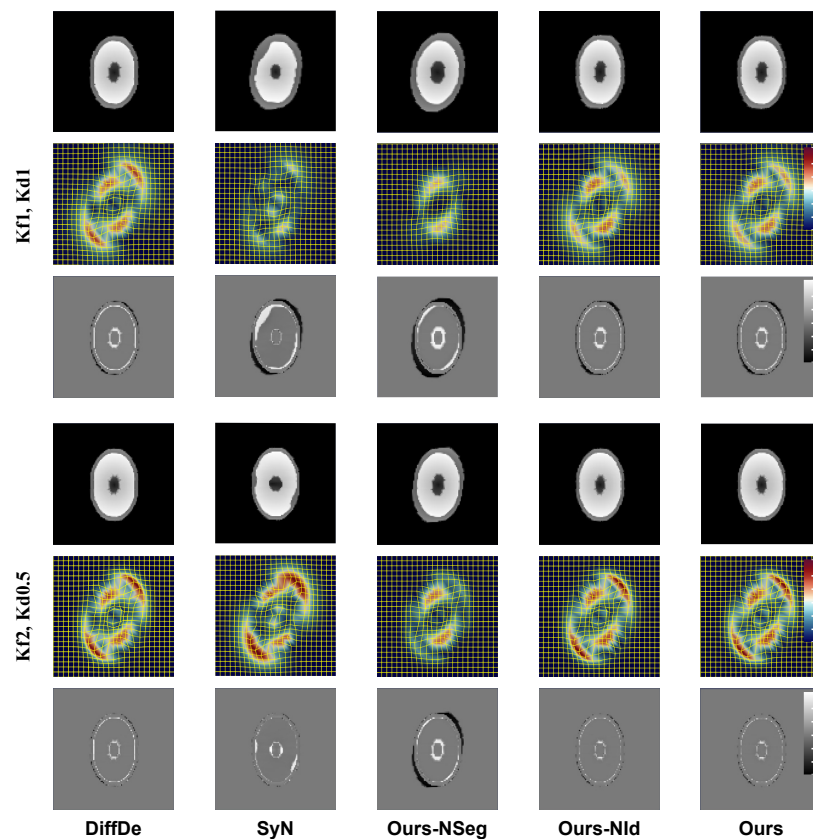


Figure 4. The qualitative results of Section 3.2 are shown. The figure has two parts, distinguishing between two kinds of smoothing parameters, i.e., **Kf1 Kd1** and **Kf2 Kd0.5**. In each part, the three rows display the warped moving images, the deformation grids, and the residual images, respectively. Different columns are the results of different methods. The color of the deformation grids, whose scale bar ranges from -4.5 to 5.8 pixels, represents the magnitude of the transformations. The color of the residual images, whose scale bar ranges from -3.0 to 3.2 , represents the difference between the intensity values of the fixed image and the warped moving images.

Thirdly, we discuss the comparison among **DiffDe**, **SyN**, and **Ours**. As described in Tables 1 and 2, **DiffDe** shows poor results in the items of **IdErr**, **M(DetJ)**, and **SMErr**, although the warped moving images of **DiffDe** are very similar to those of **Ours**. Moreover, **SyN** achieves the best reversibility. However, the warped moving images of **SyN** are not satisfactory because the shapes of the white ellipses do not maintain, as displayed in Figure 4. By contrast, the shapes of **Ours** are good, which means **Ours** can recover the deformation. Moreover, **Ours** has the best accuracy and reasonability, as revealed in Tables 1 and 2.

3.3. The Anti-Noise Experiments on the OASIS-1 Dataset

In this section, we show the robustness of our method to the noise through the anti-noise experiments. The OASIS-1 dataset [52], which we use, contains 416 subjects aged from 18 to 96. This dataset is a part of the OASIS project to make neuroimaging data freely available (<https://www.oasis-brains.org>, accessed on 31 May 2022). It is used widely in the comparison of registration algorithms [60–62]. Each subject is equipped with a T1-weighted skull-stripped image, a **BRS** of 35 brain regions, and a **WGCS**, as shown in the first three images of Figure 5. All the masks are verified by experts. The size of the images is $160 \times 192 \times 224$ voxels with a voxel size of $1 \times 1 \times 1 \text{ mm}^3$.

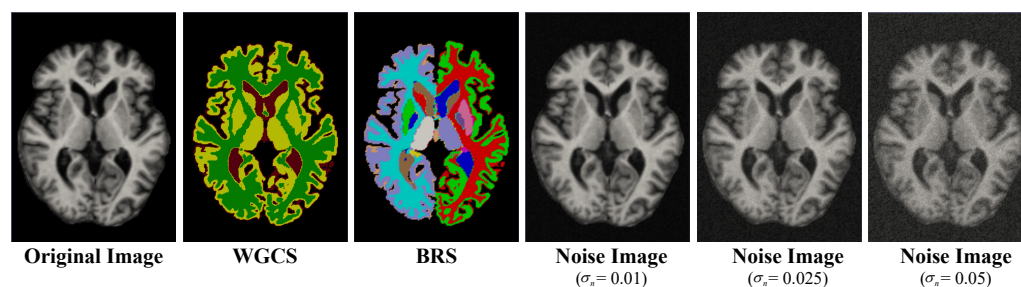


Figure 5. The axial view of both #161 in the OASIS-1 dataset and noise images are shown. The first image is the original skull-stripped image of #161, the second image is the related WGCS, and the third image is the BRS of 35 regions. The last three images display the noise images of the standard deviation $\sigma_n = 0.01, 0.025, 0.05$, respectively.

We selected five subjects in the OASIS-1 dataset randomly to avoid the influence of the sort order in the dataset. Next, we designate one subject as the fixed image and leave the other four as moving images. Specifically, the fixed image is #161, and the moving images are #227, #287, #319, and #333, respectively. We then add Gaussian noise of four standard deviations to the images, i.e., $\sigma_n = 0, 0.01, 0.025, 0.05$, where 0 means no noise. Therefore, each method performs $4 \times 4 = 16$ registration. The higher the standard deviation, the stronger the noise is, as shown in the last three images of Figure 5. We use additive Gaussian white noise because it is common in nature. After that, we carry out histogram matching to reduce the uncertainty caused by the different distributions of the intensity values in the images. Meanwhile, we reassign the intensity value of the masks. Finally, we conduct registration with $\text{numIt} = 150$. In particular, we set 10 external iterations \times 15 internal iterations in our method. The smoothing parameters are chosen to be **Kf2 Kd0.5** for all methods. The reason is that **Kf2 Kd0.5** can obtain high accuracy while maintaining good smoothness, which is suggested by the quantitative and qualitative results in Section 3.2.

Firstly, we analyze an example in which #227 and #161 are the moving image and the fixed image, respectively. The registration of this example is performed with the noise of $\sigma_n = 0.05$. We present the warped **BRS**s in Figure 6, which can show the accuracy is poor if a large difference between the warped **BRS**s and the fixed **BRS**s occurs. The results of **DiffDe** and **SyN** are not satisfactory, e.g., **DiffDe**'s and **SyN**'s volume of the left and right ventricles is larger than the fixed **BRS**'s. By contrast, **Ours** has the best results in this example because the volume and position of the brain regions are very close to the fixed **BRS**.

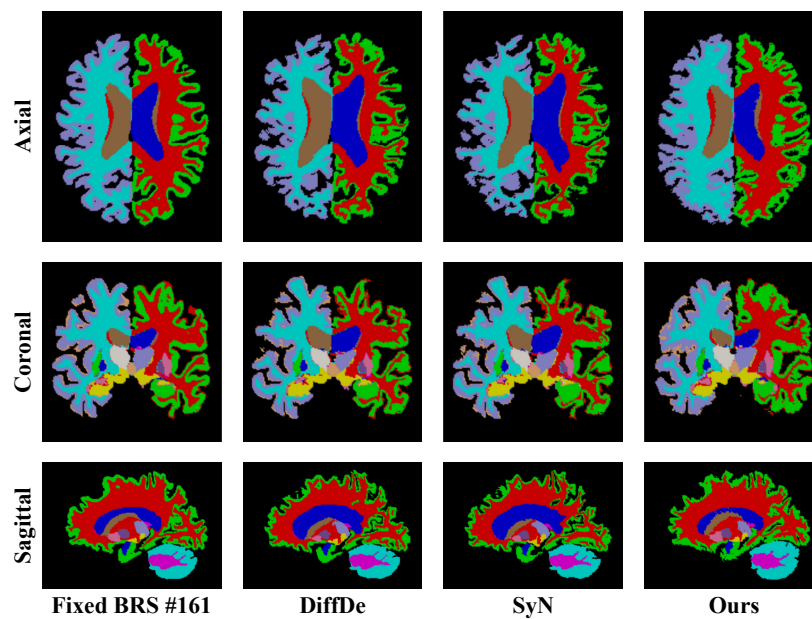


Figure 6. The qualitative results of Section 3.3 are shown. The first to third rows display the BRSs of the axial, coronal, and sagittal sections, respectively. The first column shows the fixed BRS of #161. The second to forth columns show the warped BRSs of the methods.

Secondly, we plot how the DR varies with the noise intensity in Figure 7. The high slope of the line segments indicates that the noise can affect the accuracy greatly. The stability of **DiffDe** is weak because the DR decreases rapidly when the noise is enhanced. By contrast, **SyN**'s performance is better than **DiffDe**'s, e.g., the line segments of 0.01 \rightarrow 0.025 are almost flat. The results of **Ours** are similar to those of **SyN**, but the overall performance of **Ours** is better. Consequently, **Ours** has strong robustness to the noise.

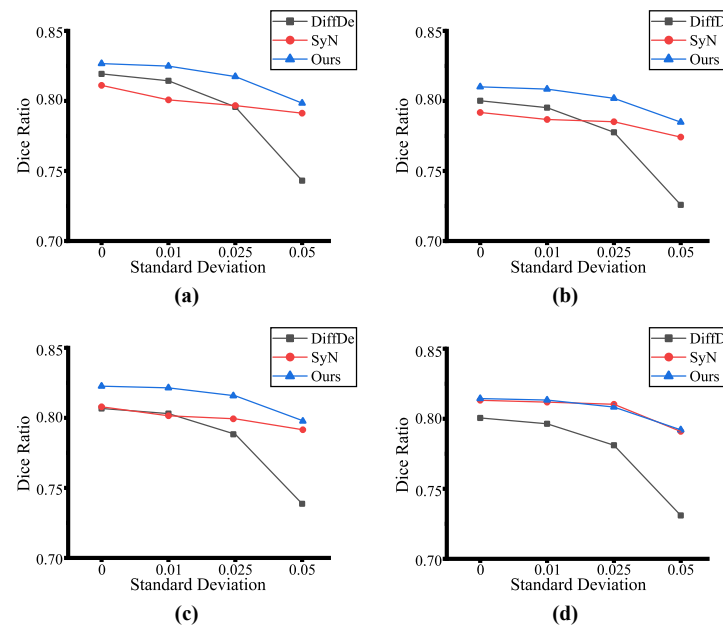


Figure 7. The quantitative results of Section 3.3 are shown. (a) The registration results from #227 to #161. (b) The registration results from #287 to #161. (c) The registration results from #319 to #161. (d) The registration results from #333 to #161. In each diagram, we plot the images of the Dice ratio with respect to the standard deviations of the noise, where 0 means no noise.

3.4. The Performance Experiments on the IBSR18 Dataset

In this section, we demonstrate the excellent comprehensive capabilities of our approach through the performance experiments. The Internet Brain Segmentation Repository (IBSR) contains T1-weighted MRI brain images of 18 subjects. The original images were preprocessed by the Center for Morphometric Analysis, Massachusetts General Hospital in Boston, U.S. [28]. We use the IBSR18 v2.0 dataset (<https://www.nitrc.org/projects/ibsr/>, accessed on 31 May 2022), in which Rohlfing et al. [53] modified the IBSR18 dataset by removing non-brain regions, etc. We can see this dataset is commonly used in the field of brain image registration [28,63–65]. Each subject is equipped with a skull-stripped image, a **BRS** of 84 brain regions, and a **WGCS**. The size of the images is $256 \times 256 \times 128$ voxels with a voxel size of $(0.837 \sim 1) \times (0.837 \sim 1) \times 1.5 \text{ mm}^3$.

We first crop the unnecessary area of the images, which changes the size into $166 \times 161 \times 128$. We also unify the voxel size to $0.97 \times 0.97 \times 1 \text{ mm}^3$. We then choose the same smoothing parameters as in Section 3.3, i.e., **Kf2 Kd0.5**. After that, we conduct registration with **numIt** = 150. In particular, we set 10 external iterations \times 15 internal iterations in our method. Finally, we select the first ten subjects in the dataset. We make each subject the fixed image and the other nine subjects the moving images. Therefore, each method performs $10 \times 9 = 90$ registration.

Firstly, we analyze an example in which #02 and #01 are the moving and fixed images, respectively. We display, in Figure 8, the moving image, the fixed image, and the warped moving images of different methods. We enlarge representative positions to analyze the difference in the results conveniently. For example, the first row of Figure 8 shows the axial sections. The result of **Ours** is the most similar to the fixed image considering the contour of the left ventricle and the left thalamus. Furthermore, we can also verify the excellent performance of **Ours** from the second and third rows of Figure 8, representing the coronal and sagittal sections of the images, respectively.

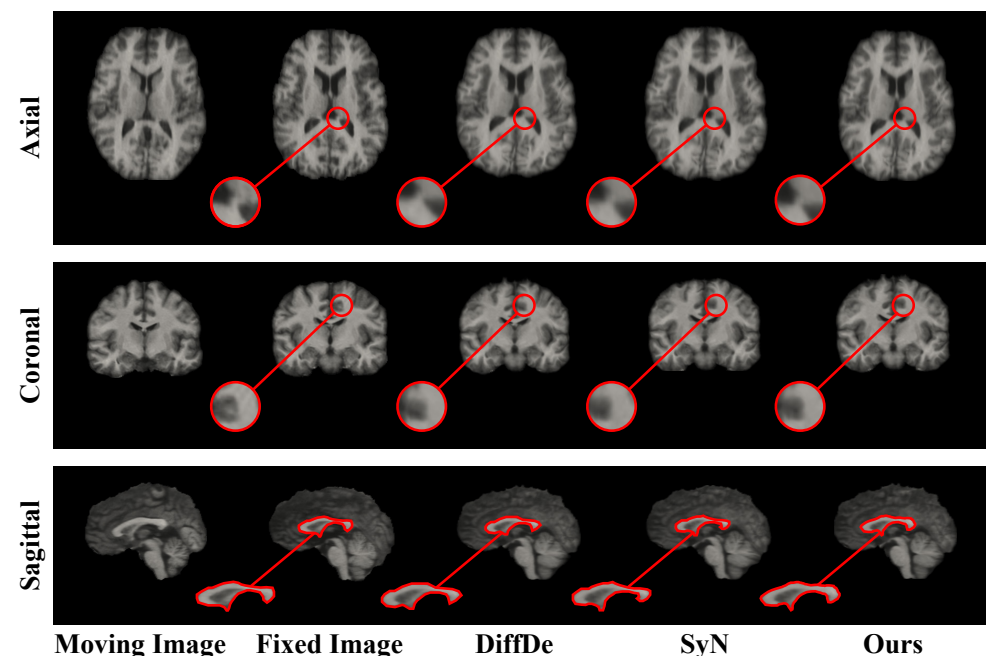


Figure 8. The registration results of an example in Section 3.4 are shown. All images are plotted in the axial, coronal, and sagittal sections. The first column displays the moving image #02, and the second column displays the fixed image #01. The third to fifth columns represent the warped moving images of different methods, i.e., **DiffDe**, **SyN**, and **Ours**, respectively.

Secondly, we can also compare the results from the volumetric plots and point cloud maps of the evaluation metrics based on the above example. We show the volumetric plots of the **DR** for each brain region after stripping the upper part of the brain, as displayed

in the first row of Figure 9. We can see that **Ours** achieves the optimal result because its color is the closest to blue. In the second row of Figure 9, we plot the volume of the **SMErr** of the transformations over the entire brain. All three methods appear to be smooth overall, but **SyN** shows more large deformations because there is more volume of red. We last display in the third row of Figure 9 the point cloud maps where the negative Jacobian determinant occurs. In contrast, **SyN** has the most points, **DiffDe** has the second most, and **Ours** has the fewest. Therefore, **Ours** shows, in this example, wonderful results considering accuracy, smoothness, and reasonability.

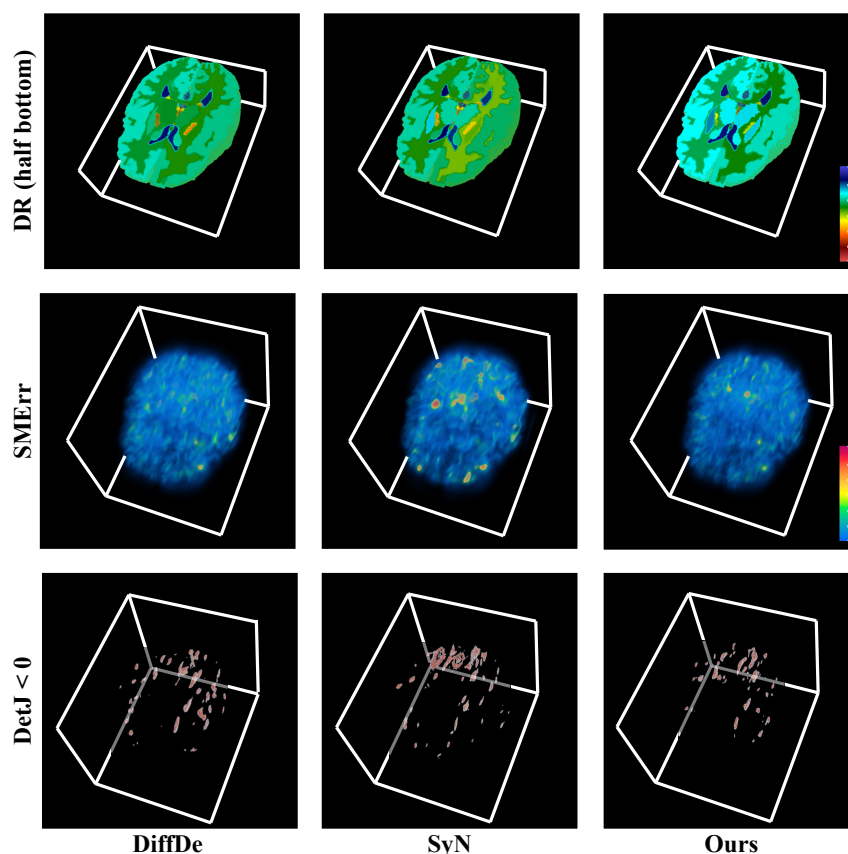


Figure 9. The qualitative results in Section 3.4, based on Figure 8, are shown. The first to third columns distinguish the results of **DiffDe**, **SyN**, and **Ours**. The first row displays the half-bottom volumetric plots of the **DR**, where the scale bar ranges from 0.7 to 0.91. The second row displays volumetric plots of the **SMErr**, where the scale bar ranges from 0 to 11.28. The third row displays the point cloud maps showing where the negative Jacobian determinant occurs ($\text{Det}J < 0$).

Thirdly, we organize the quantitative results of 90 registration in Table 3, which lists the mean and standard deviation of each evaluation metric. The results of **DiffDe** are relatively stable because its standard deviations are lower than other methods' in most items. It is worth noting that **SyN** achieves the best result of the **IdErr**, but **SyN** is not remarkable in the remaining items. By contrast, **Ours** is the best considering the **DR**, **P(DetJ)**, **M(DetJ)**, and **SMErr**, which means the results of **Ours** have excellent accuracy, reasonability, and smoothness.

Table 3. The quantitative results in Section 3.4 are shown. The results represent the mean values and corresponding standard deviations with 90 registrations. The first row lists the methods, i.e., no registration (No Reg.), DiffDe, SyN, and Ours. The second to sixth rows represents the results of the DR, IdErr, P(DetJ), M(DetJ), and SMErr, respectively. The bolded numbers are the best results among different methods.

	No Reg.	DiffDe	SyN	Ours
DR	0.605 (0.040)	0.815 (0.020)	0.811 (0.022)	0.825 (0.019)
IdErr	N/A	0.750 (0.230)	0.015 (0.019)	0.316 (0.172)
P(DetJ) (‰)	N/A	0.836 (0.442)	1.836 (1.311)	0.517 (0.460)
M(DetJ)	N/A	4.211 (0.434)	4.605 (0.541)	3.949 (0.620)
SMErr	N/A	0.045 (0.010)	0.073 (0.025)	0.035 (0.012)

4. Discussion

We verify the advantages of our method through the experimental results. The multi-label segmentation masks are added to the model as a priori information. The reassignment ensures the masks contain both the spatial information of the region boundaries and the mean intensity values in the regions. Therefore, the masks improve the alignment of the regions and robustness to the noise. Moreover, the symmetric form of the model strengthens the reversibility, reasonability, and smoothness without losing much accuracy. Furthermore, we need the masks of large regions only, which are accessible easily in practice. The masks can also be changed with different region definitions. Finally, our method has a very small computational cost and can thus obtain transformations quickly because of the SVF framework.

Our method also has some disadvantages. Firstly, the method relies on additional segmentation methods to obtain the masks. Secondly, the accuracy can be reduced if the inaccurate masks of large regions are used. Thirdly, the amount of calculation increases exponentially with the radius of N_x , which is $(2R + 1)^n$ specifically, where n is the image dimensionality and R is the radius. If the image size and dimensionality are small, enlarging the radius is a good choice, which improves the accuracy of the parameter estimation. However, selecting a large radius is not applicable for high-resolution 3D medical images.

We plan to provide the masks for the model by establishing a relating segmentation method in the future. In addition, we will research to strengthen the convergence of reversibility. We will also apply the method to multi-modality registration.

5. Conclusions

In this study, we propose a symmetric diffeomorphic image registration model based on the multi-label segmentation masks to solve the problems in brain MRI registration. We tackle the issue that existing methods pay little attention to the alignment of the region boundaries by introducing the similarity metric of the multi-label segmentation masks. It also improves the robustness to the noise. We build the model on the diffeomorphism group, with the relaxation method and the inverse consistent constraint to strengthen the smoothness and reversibility. Moreover, we help the descent of the energy function in different regions through the spatially adaptive parameters. Finally, we verify the effectiveness of our method through three experiments. Compared with mainstream methods, the approach has better accuracy and noise resistance, and the transformations are more smooth and more reasonable.

Author Contributions: Formal analysis, C.C., L.W., and S.Y.; Methodology, C.C. and S.Y.; Validation: C.C., L.W., and S.Y.; Writing—original draft, C.C.; Writing—review and editing: C.C. and S.Y. All authors have read and agreed to the published version of the manuscript.

Funding: This research is supported by the National Natural Science Foundation of China (No. 11971296).

Institutional Review Board Statement: Not applicable.

Informed Consent Statement: Not applicable.

Data Availability Statement: Not applicable.

Conflicts of Interest: The authors declare no conflict of interest.

References

- Xing, F.; Liu, X.; Kuo, J.; Fakhri, G.; Woo, J. Brain MR atlas construction using symmetric deep neural inpainting. *IEEE J. Biomed. Health Inform.* 2022, *online ahead of print*. [[CrossRef](#)] [[PubMed](#)]
- Fan, L.; Li, H.; Zhuo, J.; Zhang, Y.; Wang, J.; Chen, L.; Yang, Z.; Chu, C.; Xie, S.; Laird, A.R.; et al. The human brainnetome atlas: A new brain atlas based on connectonal architecture. *Cereb. Cortex* **2016**, *26*, 3508–3526. [[CrossRef](#)] [[PubMed](#)]
- Boveiri, H.R.; Khayami, R.; Javidan, R.; Mehdizadeh, A. Medical image registration using deep neural networks: A comprehensive review. *Comput. Electr. Eng.* **2020**, *87*, 106767. [[CrossRef](#)]
- Wang, M.; Li, P. A review of deformation models in medical image registration. *J. Med. Biol. Eng.* **2019**, *39*, 1–17. [[CrossRef](#)]
- Chen, X.; Diaz-Pinto, A.; Ravikumar, N.; Frangi, A.F. Deep learning in medical image registration. *Prog. Biomed. Eng.* **2021**, *3*, 012003. [[CrossRef](#)]
- Kybic, J.; Unser, M. Fast parametric elastic image registration. *IEEE Trans. Image Process.* **2003**, *12*, 1427–1442. [[CrossRef](#)]
- Rueckert, D.; Aljabar, P.; Heckemann, R.A.; Hajnal, J.V.; Hammers, A. Diffeomorphic registration using B-splines. In *International Conference on Medical Image Computing and Computer-Assisted Intervention*; Springer: Berlin/Heidelberg, Germany, 2006; pp. 702–709.
- Zachariadis, O.; Teatini, A.; Satpute, N.; Gómez-Luna, J.; Mutlu, O.; Elle, O.J.; Olivares, J. Accelerating B-spline interpolation on GPUs: Application to medical image registration. *Comput. Methods Programs Biomed.* **2020**, *193*, 105431. [[CrossRef](#)] [[PubMed](#)]
- Rohr, K.; Fornefett, M.; Stiehl, H.S. Spline-based elastic image registration: Integration of landmark errors and orientation attributes. *Comput. Vis. Image Underst.* **2003**, *90*, 153–168. [[CrossRef](#)]
- Cavoretto, R.; De Rossi, A. Analysis of compactly supported transformations for landmark-based image registration. *Appl. Math. Inf. Sci.* **2013**, *7*, 2113. [[CrossRef](#)]
- Liu, J.X.; Chen, Y.S.; Chen, L.F. Fast and accurate registration techniques for affine and nonrigid alignment of MR brain images. *Ann. Biomed. Eng.* **2010**, *38*, 138–157. [[CrossRef](#)]
- Bookstein, F.L. Thin-plate splines and the atlas problem for biomedical images. In *Biennial International Conference on Information Processing in Medical Imaging*; Springer: Berlin/Heidelberg, Germany, 1991; pp. 326–342.
- Wu, G.; Yap, P.T.; Kim, M.; Shen, D. TPS-HAMMER: Improving HAMMER registration algorithm by soft correspondence matching and thin-plate splines based deformation interpolation. *NeuroImage* **2010**, *49*, 2225–2233. [[CrossRef](#)]
- Dai, A.; Zhou, H.; Tian, Y.; Zhang, Y.; Lu, T. Image registration algorithm based on manifold regularization with thin-plate spline model. In *International Conference on Neural Computing for Advanced Applications*; Springer: Berlin/Heidelberg, Germany, 2020; pp. 320–331.
- Beg, M.F.; Miller, M.I.; Trounev, A.; Younes, L. Computing large deformation metric mappings via geodesic flows of diffeomorphisms. *Int. J. Comput. Vis.* **2005**, *61*, 139–157. [[CrossRef](#)]
- Younes, L.; Arrate, F.; Miller, M.I. Evolutions equations in computational anatomy. *NeuroImage* **2009**, *45*, S40–S50. [[CrossRef](#)] [[PubMed](#)]
- Vialard, F.X.; Risser, L.; Rueckert, D.; Cotter, C.J. Diffeomorphic 3D image registration via geodesic shooting using an efficient adjoint calculation. *Int. J. Comput. Vis.* **2012**, *97*, 229–241. [[CrossRef](#)]
- Singh, N.; Hinkle, J.; Joshi, S.; Fletcher, P.T. A vector momenta formulation of diffeomorphisms for improved geodesic regression and atlas construction. In *2013 IEEE 10th International Symposium on Biomedical Imaging*; IEEE: Piscataway, NJ, USA, 2013; pp. 1219–1222.
- Broit, C. *Optimal Registration of Deformed Images*; University of Pennsylvania: Philadelphia, PA, USA, 1981.
- Rueckert, D.; Sonoda, L.I.; Hayes, C.; Hill, D.L.; Leach, M.O.; Hawkes, D.J. Nonrigid registration using free-form deformations: Application to breast MR images. *IEEE Trans. Med. Imaging* **1999**, *18*, 712–721. [[CrossRef](#)] [[PubMed](#)]
- Zhang, J.; Wang, J.; Wang, X.; Feng, D. The adaptive FEM elastic model for medical image registration. *Phys. Med. Biol.* **2013**, *59*, 97. [[CrossRef](#)]
- Christensen, G.E.; Joshi, S.C.; Miller, M.I. Volumetric transformation of brain anatomy. *IEEE Trans. Med. Imaging* **1997**, *16*, 864–877. [[CrossRef](#)]
- Chiang, M.C.; Leow, A.D.; Klunder, A.D.; Dutton, R.A.; Barysheva, M.; Rose, S.E.; McMahon, K.L.; De Zubicaray, G.I.; Toga, A.W.; Thompson, P.M. Fluid registration of diffusion tensor images using information theory. *IEEE Trans. Med. Imaging* **2008**, *27*, 442–456. [[CrossRef](#)] [[PubMed](#)]
- Tian, L.; Puett, C.; Liu, P.; Shen, Z.; Aylward, S.R.; Lee, Y.Z.; Niethammer, M. Fluid registration between lung CT and stationary chest tomosynthesis images. In *International Conference on Medical Image Computing and Computer-Assisted Intervention*; Springer: Berlin/Heidelberg, Germany, 2020; pp. 307–317.
- Fischer, B.; Modersitzki, J. Fast inversion of matrices arising in image processing. *Numer. Algorithms* **1999**, *22*, 1–11. [[CrossRef](#)]
- Modersitzki, J. *Numerical Methods for Image Registration*; Oxford University Press: Oxford, UK, 2004.
- Vercauteren, T.; Pennec, X.; Perchant, A.; Ayache, N. Non-parametric diffeomorphic image registration with the demons algorithm. In *International Conference on Medical Image Computing and Computer-Assisted Intervention*; Springer: Berlin/Heidelberg, Germany, 2007; pp. 319–326.

28. Klein, A.; Andersson, J.; Ardekani, B.A.; Ashburner, J.; Avants, B.; Chiang, M.C.; Christensen, G.E.; Collins, D.L.; Gee, J.; Hellier, P.; et al. Evaluation of 14 nonlinear deformation algorithms applied to human brain MRI registration. *NeuroImage* **2009**, *46*, 786–802. [[CrossRef](#)] [[PubMed](#)]
29. Ying, S.; Wu, G.; Wang, Q.; Shen, D. Hierarchical Unbiased Graph Shrinkage (HUGS): A novel groupwise registration for large data set. *NeuroImage* **2014**, *84*, 626–638. [[CrossRef](#)] [[PubMed](#)]
30. Zhang, M.; Fletcher, P.T. Fast diffeomorphic image registration via Fourier-approximated Lie algebras. *Int. J. Comput. Vis.* **2019**, *127*, 61–73. [[CrossRef](#)]
31. Gupta, S.; Gupta, P.; Verma, V.S. Study on anatomical and functional medical image registration methods. *NeuroComputing* **2021**, *452*, 534–548. [[CrossRef](#)]
32. Fluck, O.; Vetter, C.; Wein, W.; Kamen, A.; Preim, B.; Westermann, R. A survey of medical image registration on graphics hardware. *Comput. Methods Programs Biomed.* **2011**, *104*, e45–e57. [[CrossRef](#)]
33. Chang, H.H.; Chao, Y.H. Fast volumetric registration in MR images based on an accelerated viscous fluid model. In *2020 28th European Signal Processing Conference (EUSIPCO)*; IEEE: Piscataway, NJ, USA, 2021; pp. 1284–1288.
34. Fernández-Fabeiro, J.; Gonzalez-Escribano, A.; Llanos, D.R. Distributed programming of a hyperspectral image registration algorithm for heterogeneous GPU clusters. *J. Parallel Distrib. Comput.* **2021**, *151*, 86–93. [[CrossRef](#)]
35. Ni, H.; Tan, C.; Feng, Z.; Chen, S.; Zhang, Z.; Li, W.; Guan, Y.; Gong, H.; Luo, Q.; Li, A. A robust image registration interface for large volume brain atlas. *Sci. Rep.* **2020**, *10*, 2139. [[CrossRef](#)] [[PubMed](#)]
36. Minaee, S.; Boykov, Y.Y.; Porikli, F.; Plaza, A.J.; Kehtarnavaz, N.; Terzopoulos, D. Image segmentation using deep learning: A survey. *IEEE Trans. Pattern Anal. Mach. Intell.* **2021**, *44*, 3523–3542. [[CrossRef](#)] [[PubMed](#)]
37. Haralick, R.M.; Shapiro, L.G. Image segmentation techniques. *Comput. Vis. Graph. Image Process.* **1985**, *29*, 100–132. [[CrossRef](#)]
38. Pal, N.R.; Pal, S.K. A review on image segmentation techniques. *Pattern Recognit.* **1993**, *26*, 1277–1294. [[CrossRef](#)]
39. Pham, D.L.; Xu, C.; Prince, J.L. Current methods in medical image segmentation. *Annu. Rev. Biomed. Eng.* **2000**, *2*, 315–337. [[CrossRef](#)]
40. Mahony, R.; Manton, J.H. The geometry of the Newton method on non-compact Lie groups. *J. Glob. Optim.* **2002**, *23*, 309–327. [[CrossRef](#)]
41. Malis, E. Improving vision-based control using efficient second-order minimization techniques. In *IEEE International Conference on Robotics and Automation, ICRA'04*; IEEE: Piscataway, NJ, USA, 2004; Volume 2, pp. 1843–1848.
42. Arsigny, V.; Commowick, O.; Pennec, X.; Ayache, N. A log-Euclidean framework for statistics on diffeomorphisms. In *International Conference on Medical Image Computing and Computer-Assisted Intervention*; Springer: Berlin/Heidelberg, Germany, 2006; pp. 924–931.
43. Higham, N.J. The scaling and squaring method for the matrix exponential revisited. *SIAM J. Matrix Anal. Appl.* **2005**, *26*, 1179–1193. [[CrossRef](#)]
44. Vercauteren, T.; Pennec, X.; Perchant, A.; Ayache, N. Symmetric log-domain diffeomorphic registration: A demons-based approach. In *International Conference on Medical Image Computing and Computer-Assisted Intervention*; Springer: Berlin/Heidelberg, Germany, 2008; pp. 754–761.
45. Gonzalez, R.; Woods, R. *Digital Image Processing*; Prentice Hall: Hoboken, NJ, USA, 2008.
46. Ye, X.; Chen, Y. A new algorithm for inverse consistent image registration. In *International Symposium on Visual Computing*; Springer: Berlin/Heidelberg, Germany, 2009; pp. 855–864.
47. Ying, S.; Li, D.; Xiao, B.; Peng, Y.; Du, S.; Xu, M. Nonlinear image registration with bidirectional metric and reciprocal regularization. *PLoS ONE* **2017**, *12*, e0172432. [[CrossRef](#)] [[PubMed](#)]
48. Cachier, P.; Bardinet, E.; Dormont, D.; Pennec, X.; Ayache, N. Iconic feature based nonrigid registration: The PASHA algorithm. *Comput. Vis. Image Underst.* **2003**, *89*, 272–298. [[CrossRef](#)]
49. Cachier, P.; Ayache, N. Isotropic energies, filters and splines for vector field regularization. *J. Math. Imaging Vis.* **2004**, *20*, 251–265. [[CrossRef](#)]
50. Vercauteren, T.; Pennec, X.; Malis, E.; Perchant, A.; Ayache, N. Insight into efficient image registration techniques and the demons algorithm. In *Biennial International Conference on Information Processing in Medical Imaging*; Springer: Berlin/Heidelberg, Germany, 2007; pp. 495–506.
51. Misra, D. Mish: A self regularized non-monotonic activation function. *arXiv* **2019**, arXiv:1908.08681.
52. Marcus, D.S.; Wang, T.H.; Parker, J.; Csernansky, J.G.; Morris, J.C.; Buckner, R.L. Open Access Series of Imaging Studies (OASIS): Cross-sectional MRI data in young, middle aged, nondemented, and demented older adults. *J. Cogn. Neurosci.* **2007**, *19*, 1498–1507. [[CrossRef](#)] [[PubMed](#)]
53. Rohlfing, T. Image similarity and tissue overlaps as surrogates for image registration accuracy: Widely used but unreliable. *IEEE Trans. Med. Imaging* **2011**, *31*, 153–163. [[CrossRef](#)] [[PubMed](#)]
54. Johnson, H.J.; McCormick, M.M.; Ibanez, L. *The ITK Software Guide: Design and Functionality*, 4th ed.; Kitware Inc.: New York, NY, USA, 2015.
55. Thirion, J.P. Image matching as a diffusion process: An analogy with Maxwell's demons. *Med. Image Anal.* **1998**, *2*, 243–260. [[CrossRef](#)]
56. Avants, B.B.; Epstein, C.L.; Grossman, M.; Gee, J.C. Symmetric diffeomorphic image registration with cross-correlation: Evaluating automated labeling of elderly and neurodegenerative brain. *Med. Image Anal.* **2008**, *12*, 26–41. [[CrossRef](#)] [[PubMed](#)]

57. Risser, L.; Vialard, F.X.; Baluwala, H.Y.; Schnabel, J.A. Piecewise-diffeomorphic image registration: Application to the motion estimation between 3D CT lung images with sliding conditions. *Med. Image Anal.* **2013**, *17*, 182–193. [[CrossRef](#)] [[PubMed](#)]
58. Sloots, J.J.; Biessels, G.J.; de Luca, A.; Zwanenburg, J.J. Strain tensor imaging: Cardiac-induced brain tissue deformation in humans quantified with high-field MRI. *NeuroImage* **2021**, *236*, 118078. [[CrossRef](#)] [[PubMed](#)]
59. Avants, B.B.; Tustison, N.J.; Song, G.; Cook, P.A.; Klein, A.; Gee, J.C. A reproducible evaluation of ANTs similarity metric performance in brain image registration. *NeuroImage* **2011**, *54*, 2033–2044. [[CrossRef](#)] [[PubMed](#)]
60. Sabuncu, M.R.; Yeo, B.; Leemput, K.V.; Vercauteren, T.; Golland, P. Asymmetric image-template registration. In *International Conference on Medical Image Computing and Computer-Assisted Intervention*; Springer: Berlin/Heidelberg, Germany, 2009; pp. 565–573.
61. Yang, X.; Kwitt, R.; Styner, M.; Niethammer, M. Quicksilver: Fast predictive image registration—a deep learning approach. *NeuroImage* **2017**, *158*, 378–396. [[CrossRef](#)] [[PubMed](#)]
62. Wang, J.; Zhang, M. Deepflash: An efficient network for learning-based medical image registration. In Proceedings of the IEEE/CVF Conference on Computer Vision and Pattern Recognition, Seattle, WA, USA, 14–19 June 2020; pp. 4444–4452.
63. Lorenzi, M.; Ayache, N.; Frisoni, G.B.; Pennec, X. LCC-Demons: A robust and accurate symmetric diffeomorphic registration algorithm. *NeuroImage* **2013**, *81*, 470–483. [[CrossRef](#)]
64. Fan, J.; Cao, X.; Xue, Z.; Yap, P.T.; Shen, D. Adversarial similarity network for evaluating image alignment in deep learning based registration. In *International Conference on Medical Image Computing and Computer-Assisted Intervention*; Springer: Berlin/Heidelberg, Germany, 2018; pp. 739–746.
65. Niethammer, M.; Kwitt, R.; Vialard, F.X. Metric learning for image registration. In Proceedings of the IEEE/CVF Conference on Computer Vision and Pattern Recognition, Long Beach, CA, USA, 15–20 June 2019; pp. 8463–8472.